SpinyHand: Contact Load Sharing for a Human-Scale Climbing Robot

Shiquan Wang[*][†]
Hao Jiang[*]
Tae Myung Huh
Danning Sun
Wilson Ruotolo
Matthew Miller
Will R. T. Roderick
Graduate Research Assistant
Dept. of Mechanical Engineering
Stanford University
424 Panama Mall, Bldg 560
Stanford, California, 94305 USA

Hannah S. Stuart
Assistant Professor
Dept. of Mechanical Engineering
University of California
2521 Hearst Avenue
Berkeley, California, 94709 USA
hstuart@berkeley.edu

Mark R. Cutkosky
Professor
Dept. of Mechanical Engineering
Stanford University
416 Escondido Mall, Bldg 550
Stanford, California, 94305 USA
cutkosky@stanford.edu

We present a hand specialized for climbing unstructured rocky surfaces. Articulated fingers achieve grasps commonly used by human climbers. The gripping surfaces are equipped with dense arrays of spines that engage with asperities on hard rough materials. A load-sharing transmission system divides the shear contact force among spine tiles on each phalanx to prevent premature spine slippage or grasp failure. Taking advantage of the hand's kinematic and load-sharing properties, the wrench space of achievable forces and moments can be computed rapidly. Bench-top tests show agreement with the model, with average wrench space errors of 10-15%, despite the stochastic nature of spine/surface interaction. The model provides design guidelines and control strategy insights for the SpinyHand and can inform future work.

1 Introduction

The ability of robots to climb walls, cliffs and other steep surfaces would be beneficial for various applications including planetary exploration and search and rescue. In recent years, a number of climbing robots have used claws or arrays of miniature spines to climb steep and even vertical surfaces like concrete and stucco walls [1–12]. Most of these platforms are limited to relatively uniform surfaces. A large robot, with long legs, can traverse complex surfaces by stepping over obstacles and bridging gaps. However, it becomes increasingly challenging to obtain sufficient traction with increasing robot size, denoted by L, because mass grows as L^3 while foot contact area grows as L^2. Failure can be catastrophic for a large climbing robot when it falls from heights of just a meter.

SpinyHand is part of a collaboration among Duke University, Stanford University, and the University of California Santa Barbara to enable the 100 kg *RoboSimian* [13] to climb steep rocky surfaces. To support large loads on surfaces that are not relatively flat, the design presented here and shown in Fig. 1 combines spine arrays with an anthropomorphic, multifinger hand that is articulated to mimic rock climber strategies. The spines do not penetrate the surface but interact with surface features to provide large contact forces.

In the following sections, we briefly introduce the spine technology utilized in this work and review current multifinger grasp modeling strategies. Section 2 introduces the SpinyHand design, including the classification of grasping strategies inspired by human rock-climbers. Passive load

---

[*]At the time of publication, this author is affiliated with Flexiv Robotics, Ltd., 4500 Great America Pkwy, Santa Clara, Califronia 95054.

[†]Address all correspondences to this author: shiquan.wang@flexiv.com.

Fig. 1: SpinyHand grasping a pumice rock. The contact areas are covered in microspines to support large tangential forces.

sharing among the contacts allows the hand to sustain high external forces and moments on convex surfaces. Design of the fingers and palm is described in Sections 3 and 4 respectively, with special attention given to spine engagement. Section 5 extends the analysis for predicting overall force and moment capabilities as a function of finger parameters and the curvature of the grasped surface. Initial model validation is conducted with bench-top experiments in Section 6. Trials focus on low curvature surfaces, for which the spines provide the greatest advantage in comparison to conventional grippers or hands. Section 7 discusses additional design and control considerations, using simulated examples. Section 8 gives recommendations for future work.

1.1 Spines for Climbing

Spines are an evolving technology that enable robots to attach to hard, rough surfaces. Inspired by the tarsal spines of insects [14], they can catch on small asperities (bumps and pits) on surfaces. On aggregate, over many spines, this engagement can sustain large contact forces. The climbing robots cited in the last section often use elastic mechanisms that allow each spine to settle on an asperity and distribute the overall load force among groups of spines [1,15]. However, when scaling to large robots this approach requires impractically large contact areas, which become awkward to control and can prevent attachment to contoured surfaces.

A higher density of spine contact is therefore required. As modeled in [16], linearly-constrained spines consist of arrays of small, sharp spikes that slide freely normal to the substrate, allowing them to conform to local contours. Dense packing allows for high contact stresses, although the variation in loading between spines may be higher than with previous designs. Unlike typical frictional contact, the spine arrays provide high shear forces on rough surfaces with little or no normal force applied. A patch of spine-equipped tiles with half the surface area of the SpinyHand presented in this paper could hold up to 70kg on a flat concrete wall [17].

1.2 Multifinger Grasping

Multifinger grasping has been studied extensively; for recent reviews of grasp analysis and hand design, see [18] and [19], respectively. Much of the grasping literature focuses on identifying contact locations and grasp forces to achieve a stable or optimal grasp [20–22] but the mechanics of spine contact fundamentally alter grasping performance and analysis. While the hand must still conform to surfaces, grasp strength – the hand's ability to resist pull-out forces – no longer depends on frictional contacts ($F_t \leq \mu F_n$). Instead, the maximum tangential force at each spine-array is a function of contact conditions (e.g. roughness) and material strength; grasp strength is nearly unchanged over a wide range of positive normal contact forces, as described in [16,17,23]. It follows that this work focuses on distributing tangential, not normal, forces in Section 3.1 and 4.1. This tangential load sharing is accomplished with a single tendon loading all spine tiles on each finger. Although the objective is different, similar concepts have been presented for balancing torques among the joints of an underactuated hand (e.g. [24,25]).

The basic mathematical framework in the literature for describing a grasp in terms of links, joints, contacts, and tendon tensions remains valid and useful. The central challenge consists of an optimization problem: one must simultaneously minimize the energy of the hand system while also satisfying contact geometry and force constraints. Solvers for such problems typically require convex constraints, such as Coulomb friction contact. This requirement is not satisfied by spine tile contact, for which the loading limits form a non-convex boat-shaped hull [16]. One computational solution uses a mixed-integer linear programming method, accelerated by branch-and-bound and hierarchical convex decomposition methods [26]. Alternatively, in this paper, we take advantage of the load-sharing design of the fingers such that the tangential force at each contact is known immediately from the tendon tension. This simplifies the grasp analysis, as described in Section 5.4.

2 Overall Design

The hands must robustly grip under heavy loading conditions of up to 50 kg (50% of RoboSimian's total mass). In order to do so, they should provide: (i) adaptability to a wide variety of terrain features and (ii) good contact quality on a diverse set of surfaces.

Human rock climbers adapt to a variety of terrains; sloper (open-hand), crimp and pinch gripping techniques work effectively on geological features such as rounded slopes, cracks, edges, and ridges [27–30]. As shown in Fig. 2, the four-finger anthropomorphic SpinyHand can perform all the aforementioned grasps. The under-actuated fingers are each curled by a single tendon. They switch from a parallel (sloper and crimp) pose to an opposed (pinch) configuration by rotating the two outer fingers 180° at the base. Articulated fingernails help to cling on shallow ledges.

Hands disproportionately affect the inertia of a robot's limbs, so designers often reduce weight by using differen-
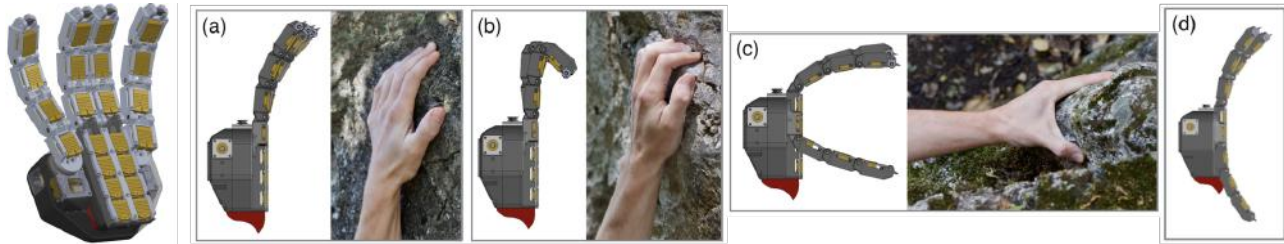
Fig. 2: (left) SpinyHand CAD rendering shows 22 spine-laden tiles in yellow distributed among 4 independent fingers and a palm. (right) Rock climbing techniques (a-d): (a) sloper grasp on a gently curved surface; (b) open hand/half crimp grasp on an edge; (c) pinch grasp on a narrow feature; (d) pose between a sloper grasp and pinch. (d) is not commonly used by human rock climber but can be helpful for SpinyHand to envelop large-curvatures.
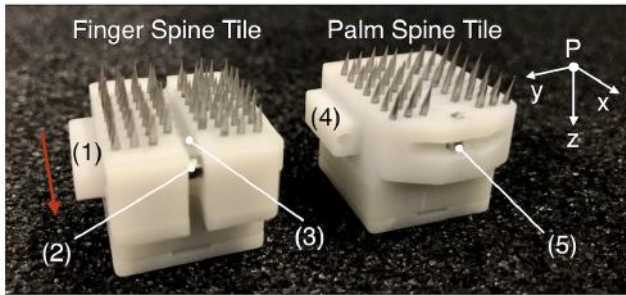

Fig. 3: Spine tile design: (1) sliding block for prismatic motion of the finger spine tile along x axis; (2) fixed pulley (horizontal metal rod); (3) groove for tendon routing; (4) sliding channel for palm tile; (5) fixed pulley (vertical metal rod). The red arrow indicates the sliding and loading direction. The tile coordinates are consistent with the finger phalanx coordinates P.

tials or clutches and multiplexing mechanisms to drive multiple fingers with fewer motors. However, when considering the benefits of brakes or clutches one must also consider how the hand responds when a grasp failure occurs. Spinyhand's fingers must react immediately and independently to asperity breakage and slippage, allowing the posture to readjust without detaching and causing the robot to fall. In the case of SpinyHand, a separate 20 W motor is dedicated to each finger with a 236:1 gear ratio that provides a maximum tendon tension of approximately 700 N, accounting for friction.

Although the transmission ratio is relatively high, there is enough compliance in the tendon and tile system to reduce the chances of tendon breakage when slips or impacts occur. The fingers and palm are machined from 7075 Al alloy and are sufficiently robust to survive impacts and grasp failures. The entire hand has a mass of 2.6 kg and each finger can produce up to 600 N at each fingertip. For implementation details, see Appendix 9.1.

When climbing on large rocky features, a hand is unlikely to achieve grasp form-closure; contact properties between the hand and the surface ultimately limit grip security. Most existing anthropomorphic hands use patches of frictional material to improve the contact interface, and push or squeeze on surfaces to achieve force-closure. This approach is insufficient for a 100 kg robot "palming" vertical features because lateral forces are very high, and squeezing harder pushes the robot away from the wall. The linearly-constrained spines on SpinyHand engage with many small surface asperities, and can provide large normal and shear attachment forces [16]. The hand is covered with twenty-two spine tiles (pictured in Fig. 3), spread throughout the palm and fingers. Tendon-based loading mechanisms distribute contact forces, as described in the next section.

3 Spined Fingers
3.1 Prismatic Phalanx

Four identical tendon-driven fingers with pin joints provide high torsional rigidity, a slender form factor, and a wide extended pose in order to grip flat surfaces. The inner surface of each phalanx is covered with spines, which most effectively provide attachment when also loaded in shear [16]. As such, the actuated contact forces should have a lateral component directed along the finger, similar to grippers that use directional adhesion [31,32].

As shown in Fig. 4, each phalanx consists of a frame and a sliding spine tile. Linear travel along each phalanx allows the tiles to catch asperities. A pair of extension springs preload the tile proximally when the fingers are open, but bias the tile distally when the tile is actuated against a surface. The tile's pulley axis (a fixed metal rod on the spine tile) is parallel to the finger joint axis, and a groove on the tile surface provides a path for the tendon. A single tendon sequentially routes around both the joint and tile pulleys, actuating spine and finger motions simultaneously. The shear component of each contact thus grows proportionally with the finger joint torque and tendon tension. Contact loading conditions, such as the ratio between shear and normal components, are determined by pulley sizes. This mechanism influences grasp modeling in Section 5.

3.2 Fingernail and finger closing sequences

An articulated fingernail, built into the distal end of each digit, is designed for clinging on very shallow edges or finger holes where the main phalanx cannot fit. Structured around another pin joint, it is preloaded by a pair of soft springs. To perform clinging, fingernail actuation occurs while the fingers are straight. With high-static-load joint bushings and sufficient structural strength of spine tiles and phalanx frames (verified with FEA), the entire finger can sustain more than 500 N shear load when clinging to terrain features with the fingernail. To prevent this ultrashort phalanx from interfering with the main finger engagement, pushing the distal phalanx away from the surface, the fingernail rotates a full 180° to retract before the tendon tension is large enough to
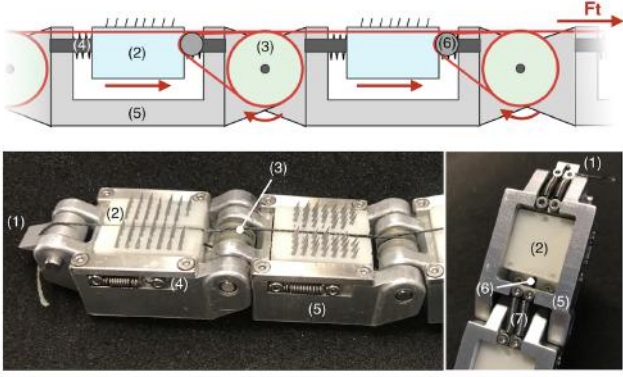
Fig. 4: Diagram and pictures of the finger: (1) fingernail; (2) spine tile; (3) joint pulley; (4) phalanx extension spring; (5) phalanx frame; (6) phalanx pulley; (7) joint extension spring. F_t is the tendon force. The tendon (red) routes around each joint pulley and phalanx pulley, so that F_t simultaneously curls the finger and slides the spine tile along the phalanx.
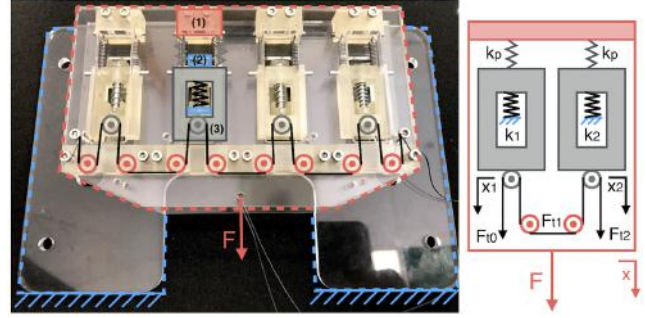

Fig. 5: Left: Palm experiment setup. Right: diagram of a 2-tile system. Parts with boundaries or shades in the same color are mounted together as single moving parts. Two tiles in gray are preloaded by springs (stiffness k_p) mounted to a moving palm frame in red. The tiles have contact stiffness k_1 and k_2 with respect to the ground in blue. A tendon routes over pulleys on the tile (gray) and palm frame (red). Local tendon tensions F_{t1} and F_{t2} may be different due to friction on pulleys between adjacent tiles. x_1, x_2 and x are global displacements of the tiles and palm frame respectively.

actuate the rest of finger joints.

After the fingernail retracts and hits its hard stop, the rest of finger starts to curl starting from the proximal to distal phalanges. This approach, largely implemented with spring elements in the fingers, prevents grasp ejection due to premature distal curling [33,34]. Only after all fingers have settled on the surface should the prismatic phalanges start to slide and load the surface, otherwise the spine tiles can no longer be actuated to generate shear contact forces. The fingernail joint spring is the softest (0.025 Nm/rad). Joint springs are slightly stiffer (0.05 Nm/rad). They must be strong enough to prevent finger sagging due to gravity and inertia, but allow full finger closing before the prismatic phalanges slide. Spine-tile springs are the strongest (11.5 N/mm), yet must not inhibit prismatic motion given actuator capabilities and motion requirements for reliable surface engagement. Spring preloads can also be used to tune the motion sequences without diminishing strength, as noted in [35].

4 Spined Palm

Based on the spine array in [17], the SpinyHand palm is large, flat and covered with spine tiles (11×6 cm with over 300 spines). Shafts support the eight tiles while allowing them to slide in the palm. Springs hold the tiles in place until spines catch on usable terrain features. A single tendon routes around all pulleys on the spine tiles and palm in order to distribute the load to all spine tiles relatively evenly. However, because the pulleys are polished stainless steel rods, there is some friction, which produces some variation in loading. As seen in the next section, a small amount of friction is actually desirable to increase robustness because it allows stiffer and stronger tile-surface contacts to assume more of the load.

4.1 Load-sharing with friction

Load sharing creates the effects that spines are additive and that tiles which happen to catch asperities on first contact do not take the brunt of the load. The strategy of attaching

multiple tiles to a single tendon would, in the case of zero friction, produce exactly the same tangential force at each tile. With friction, this is no longer the case.

For simplicity, two adjacent spine tiles are modeled, represented in Fig. 5. Each tile (grey) is preloaded by springs (black, with stiffness k_p) anchored to the palm (red) and engaged to the surface via a contact stiffness (black, with stiffnesses k_1, k_2). The loading force on the palm, F, results in tendon tensions (F_{t0}, F_{t1}, and F_{t2}) and displacements of palm and tiles (x, x_1, and x_2), respectively. The coefficient of friction associated with each pair of tendon tensions is denoted by μ and assumed constant. Given all the spring stiffnesses, four equations describe the force balance for the two tiles and two pairs of tendon tensions. Palm and tile displacements are also constrained by the total tendon length. A relation can be found between any two unknowns among x, x_1, x_2, F_{t0}, F_{t1} and F_{t2}). Note that the tendon force balancing equation is friction-direction dependent. Details of the derivation can be found in Appendix 9.2.

Solving the equations for contact forces as a function of overall palm travel, x, gives:

$$
\begin{cases}
F_1 = \frac{2(2+\mu)k_1 k_2 + 4k_p k_1}{(2-\mu)k_1 + (2+\mu)k_2 + 4k_p} x \\
F_2 = \frac{2(2-\mu)k_1 k_2 + 4k_p k_2}{(2-\mu)k_1 + (2+\mu)k_2 + 4k_p} x
\end{cases}
\tag{1}
$$

We assume that the tile with less surface engagement, and thus lower contact stiffness, will limit the pair's overall performance. The tendon/pulley friction, μ, causes the load to shift to the stiffer contact, which has caught the surface more securely. Ideally, $F_1/k_1 = F_2/k_2$ in order to distribute the load according to each tile's force limit. The desired coefficient of friction becomes:

$$
\mu = 2\frac{k_1 - k_2}{k_1 + k_2}
\tag{2}
$$

For a pair of tiles with a 2:1 force limit ratio, moderate fric-

tions with μ no larger than 2/3 help distribute the load more appropriately. We can estimate the overall 2-tile palm force limited F by the worst engaged tile's displacement, indicated here as x_2:

$$F = \frac{4k_1 k_2 + 2k_p k_1 + 2k_p k_2}{(2-\mu)k_1 + 2k_p} x_2. \qquad (3)$$

4.2 Experiments and Results

Two- and four-tile load sharing systems are used to validate the effect of transmission friction. As shown in Fig. 5 for the four-tile case, interchangeable compression springs mounted between a grounded acrylic board (blue) and the tiles (grey) simulate contact stiffnesses. An acrylic palm frame (red) holds the transmission pulleys and extension springs. All pulleys can be switched from fixed rods (μ empirically determined to be 0.34 for Dyneema tendons) to bearing-supported pulleys (μ is negligible). The force limit is simulated with a hard stop on the softest contact spring. Combinations of three contact stiffness springs are used: 1.4, 2.2 and 4.9N/mm. As shown in Fig. 6, experimental results with the two-tile system are consistent and match the model predictions within 5%. Introducing increased pulley friction, improves maximum load by at least 14%.

The model for systems with more tiles is complex due to the undetermined friction direction at each pulley; moderate tendon friction improves load sharing only between each adjacent pair of tiles. Nonetheless, friction is helpful, par-

ticularly when there are substantial discrepancies in contact quality across all tiles. For example, in experiments for a 4-tile system (Fig. 7), tendon friction improves loading limits in all 8 configurations by at least 24%.

5 Modeling Multifinger Grasping with Spines

Grasp strength estimation can guide new hand designs, selection of terrain handhold techniques, hand control, and robot motion planning. However, spine attachment produces non-convex frictional contacts, a property that makes grasp models difficult to solve [36]. This section presents an efficient approach to 3D modeling grasping with SpinyHand. We start by computing contact forces for given actuation forces, ignoring internal friction in the hand. We then consider the effect of friction in the hand in Section 5.2.

5.1 Contact Forces

The first step is solving contact forces on a single SpinyHand finger given actuation (tendon) force, finger design, and grasp surface geometry. Assuming no friction in the hand and a single contact on each phalanx, a simplified diagram demonstrates how contacts are distributed during grasping (Fig. 8). Three coordinate systems are used in the model: (1) palm coordinates (global, G); (2) finger coordinates with the z-axis the same as that of the palm coordinates and with x-z on the finger plane (F); (3) phalanx coordinates located at each phalanx (P). The model in this section is in the x-z finger plane.

Utilizing geometry constraints of the surface, joint positions of an n-phalanx finger q and the corresponding contact locations c can be computed with a bottom-up approach, from the proximal to distal phalanx. Let $q = [q_1 q_2 \ldots q_n]^T$ be the joint positions and $c = [c_1 c_2 \ldots c_n]^T$ be the contact positions, where c_i is the position along the x-axis of the phalanx
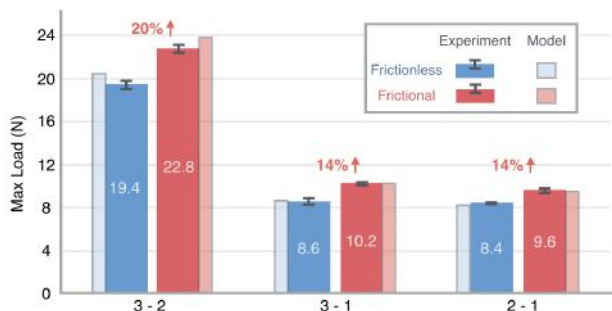

Fig. 6: Predicted and experimental maximum load of a two-tile system. Horizontal axis shows the contact spring configurations (springs 1, 2 and 3 have stiffness of 1.4, 2.2 and 4.9N/mm respectively). Five measurements are conducted for each spring configuration. The percentage in red shows how much friction can improve the loading capacity.
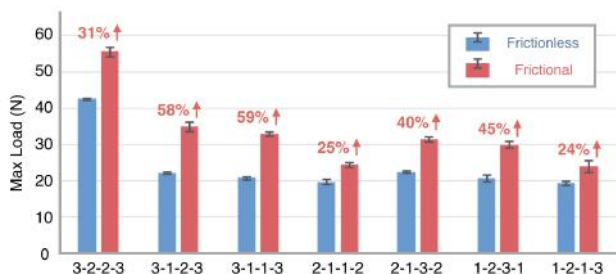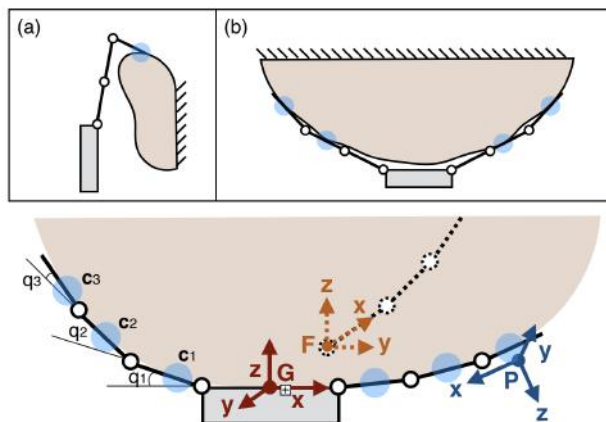

Fig. 7: Empirical maximum load of a four-tile system with and without friction. Horizontal axis shows the contact stiffness spring configurations, with the spring type sequence starting from the left.

Fig. 8: Three coordinates are used in the hand model: 1) palm (global) coordinates G; 2) finger coordinates F; 3) phalanx coordinates P. Blue dots indicates the contact locations. c_i and q_i are contact forces and joint angles. A third finger is behind the grasping surface and therefore displayed with dotted lines. The top diagrams show: (a) crimp grasp with only distal phalanx contact; (b) pinch/sloper grasp with proximal contacts broken.

frame i.[1]

At equilibrium, torques due to contact forces, tendon actuation and joint springs should balance:

$$J(q,c)^T f_c + f_t r - K_r q - p_r = 0 \qquad (4)$$

where J is an expanded Jacobian matrix $[J_1 J_2 \ldots J_n]$, with J_i being the Jacobian matrix with respect to contact on the ith phalanx. f_c is a column list of the contact forces $f_c^{(i)}$ (column vector) for phalanx i. f_t is a scalar value of the tendon force. r and p_r are, respectively, column vectors of pulley radius and preload torque for each joint. The joint stiffness matrix K_r is a diagonal matrix containing all of the joint spring stiffnesses of the elements being considered.

The floating tiles on each phalanx introduce another group of force balancing constraints:

$$P_x f_c + f_p(c, f_t) - K_p d - p_p = 0 \qquad (5)$$

where P_x is a projection matrix for contact force on each phalanx in the x-axis of its local coordinates. f_p is a column vector of the forces along the x-axis of the spine tile due to tendon actuation. Note that this force may change as the phalanx slides and affects the tendon angles on the tile pulley. d is a column of prismatic phalanx travels from their initial positions. Similar to the structure of Eqn. 4, K_p and p_p denote tile spring stiffness and preload force on each phalanx. The above equations can be rewritten compactly as:

$$A f_c = b \qquad (6)$$

where

$$A = \begin{bmatrix} J^T \\ P_x \end{bmatrix} \quad and \quad b = \begin{bmatrix} K_r q + p_r - f_t r \\ K_p d + p_p - f_p(c, f_t) \end{bmatrix} \qquad (7)$$

Matrix A is square and invertible, therefore contact forces f_c and can be solved for efficiently. We note that the prismatic phalanx design enables this approach and that solutions do not depend on the structural stiffness of the hand, which is often difficult to characterize.

5.2 Finger Friction

The above model neglects friction within the hand. In SpinyHand, friction is primarily in the tile pulleys. As the fingers close, this friction reduces the tendon tension f_t sequentially along the finger, from proximal to distal. The magnitude of the friction force is proportional to tendon tension and can be included by modifying b:

$$b = \begin{bmatrix} K_r q + p_r - f_t M r \\ K_p d + p_p - M f_p(c, f_t) \end{bmatrix} \qquad (8)$$

where M is a friction matrix with diagonal elements of $[1, (1-\mu), \ldots (1-\mu)^{n-1}]$, and μ is the lumped coefficient of friction between adjacent phalanges.

Without friction, any change of load will cause the finger to adjust its posture, moving the tendon. With friction, the motions are resisted so that Eqn. 5 is not satisfied. Before the tendon starts to slide friction should balance any change in the tangential contact forces df_{ci} along the local x axis. The friction matrix in Eqn. 8 should be modified: each diagonal element is replaced by $(1 + df_{ci}/f_{pi})$ and bounded by $(1 \pm \mu)$ when the tendon starts to slide. Appendix 9.3 provides details on solving for df_{ci}.

5.3 Finger and Grasp Stiffness

The wrench of a finger settled on a surface with respect to the global coordinate frame w_f is computed with the wrench matrix W_f; 2D forces on the finger plane are transformed to a 6D wrench with respect to the palm:

$$w_f = W_f f_c \qquad (9)$$

Small displacements of the 6D finger position x_f (finger base, origin of finger coordinates) affect w_f. The grasp wrench w_g is the sum of all finger wrenches at the wrist:

$$w_g = \sum_i^n w_{fi} \qquad (10)$$

where w_{fi} is wrench of the ith finger in a n-finger hand.

Grasp and finger stiffness matrices express the effects of small motions at the wrist and fingers on forces at the wrist and finger contacts, respectively [37]. The finger stiffness matrix, $K_f = \partial w_f / \partial x_f$, is a combination of two elements: motions in the plane of the finger and structural stiffness out of the plane. Finger stiffness components are numerically computed based on changes in f_c and w_f (using Eqn. 6 and Eqn. 9) as finger position x_f is infinitesimally shifted along different finger DOFs (x, z, and θ_y in finger coordinates). Tendon force f_t may depend on x_f when computing K_f, depending upon different tendon actuation schemes (e.g. position control). Structural stiffness components along the other three DOFs in finger coordinates are simplified by assuming linear beam elasticity. The grasp stiffness matrix K_g is defined similarly to K_f, with grasp position x_g defined as the palm coordinates.

5.4 Grasp Wrench and Wrist Motion
5.4.1 Forward solution

Given the configuration of a grasp x_g (6D position and orientation), it is straightforward to compute the grasp wrench w_g using Eqn. 6, 8, 9 and 10, given actuator forces.

5.4.2 Inverse solution

Solving in reverse from w_g to x_g is useful for grasp planning but more complicated; small changes in forces or motions applied at the wrist can produce substantial changes in

---

[1] The subscript denotes finger/joint number starting at the proximal end of the chain. The same convention applies to other variables. Every upper case, bold lower case and regular lower case symbol represents matrix, vector and scalar respectively.

the contact forces and compliant deflections at the contacts, The gradient of w_g with respect to x_g can be represented with numerical estimates of K_{fi} and J_{fi}:

$$dw_g = \sum_{i=1}^{n} K_{fi} J_{fi} dx_g = K_g dx_g \qquad (11)$$

where J_{fi} is the twist transformation matrix [22] from palm coordinates to coordinates of the ith finger:

$$dx_{fi} = J_{fi} dx_g \qquad (12)$$

and dx_{fi} and dx_g are the twists of the finger and the hand, respectively. Finger positions and contact forces can be solved with a gradient descent search; increments of x_g are computed iteratively by inverting the grasp stiffness matrix with numerical estimation.

The gradient descent search applied in this backward approach may not converge for certain hand configurations, because matrix A in Eqn. 6 is ill-conditioned when solving for K_f ($cond(A) > 270$ in all trials). A small change in the finger's pose (finger base position x_f) can result in a large change in the contact forces f_c, as noted in the experiments in Section 6. Smaller search steps typically resolve this issue, but the backward approach is less efficient than the forward approach due to its search-based solver and step constraint.

5.5 Grasp failure

We define grasp failure as spine detachment at any single contact patch; grasp failure may be catastrophic for a climbing robot, motivating this conservative approach. For each contact, an established 3D model [16] is used to estimate the loading limit of a linearly-constrained spine array. For better efficiency we linearize the spine model as a function of loading direction:

$$f_s = s(v) \qquad (13)$$

where f_s is the magnitude of failure force and v is a unit vector defining loading direction. Details of the model are described in Appendix 9.4 and empirically verified in Section 6. For concision, the condition for grasp failure is denoted by $f_c > f_s$.

SpinyHand's grasps typically fail in one of two ways: over-actuating the fingers (internal) or exceeding an allowable wrench applied at the wrist (external). In the former case we assume the configuration of the fingers is constant, in the latter case they are subject to compliant motions resulting from the external wrench.

5.5.1 Fixed-wrist grasp failure

Internal grasp failure is simulated with a fixed wrist position. Increasing finger tendon forces will eventually cause some of the prismatic phalanges to exceed shear attachment

limits and start to slide across the contact surface. We refer to this failure mode as *fixed wrist grasp failure*. This failure mode also applies if the actuators are controlled to keep the overall configuration of the fingers constant despite variations in loading.

Because tendon loading angle of the finger tile remains relatively constant, the tile preloading force is approximately proportional to the tendon force. Simplifying $f_p(c, f_t)$ as $f_t c_p$ where c_p is a scalar, Eqn. 6 can be rewritten:[2]

$$f_c = A^{-1} \begin{bmatrix} K_r q + p_r \\ K_p d + p_p \end{bmatrix} - A^{-1} f_t \begin{bmatrix} r \\ c_p \end{bmatrix} \qquad (14)$$

$$= c_{sys} + f_t c_{act}$$

Finger contact forces f_c are a superposition of two vector components. The system component c_{sys} is a constant part of the contact forces caused by passive spring elements in the design. The actuation component c_{sys} is the part in f_c that can be scaled up proportionally by tendon force. As discussed in Section 3, joint spring stiffnesses (functions of K_r and p_r) are relatively small in the actual design, which causes vectors in c_{sys} to have similar directions as c_{act}. The directions of contact forces f_c are dominated by c_{act} and remain almost constant with variations in the tendon force f_t, especially when f_t is large. By assuming fixed loading angles on the phalanx spine tiles, the phalanx closest to spine contact failure (imth phalanx) can be found with Eqn. 13. The maximum tendon force $f_{t(max)}$ that causes the fixed-wrist grasp failure is solved by iterating Eqn. 14 and 15:

$$f_{t(max)} = \frac{1}{\|R_{im} f_c^{(im)}\|} s\left(\frac{R_{im} f_c^{(im)}}{\|R_{im} f_c^{(im)}\|} \right) f_{t(max)} \qquad (15)$$

where R_{im} is the rotation matrix which transforms contact force on phalanx im to the local phalanx coordinate frame. The solution typically converges within a few iterations due to approximate collinearity between c_{sys} and c_{act}.

5.5.2 Floating-wrist grasp failure

External grasp failure is modeled by loading the wrist with increasing wrenches while keeping finger motors stationary. The wrench moves the wrist slightly, causing small changes in the finger poses and varying the contact forces until $f_c > f_s$ at one of the contacts. The corresponding limiting wrench is found by sweeping the wrench direction and monitoring the resultant contact forces using the inverse solution (Section 5.4.2) until contact failure occurs (Eqn. 13).

5.6 Grasp Wrench Space

The grasp wrench space describes all possible forces and torques a grasp can generate. When computing such a space, optimization-based models, such as [20,21,36,38], require extensive computation time to construct the wrench

---

[2] f_p is a column vector of 2 if joint and tile pulleys have the same radii
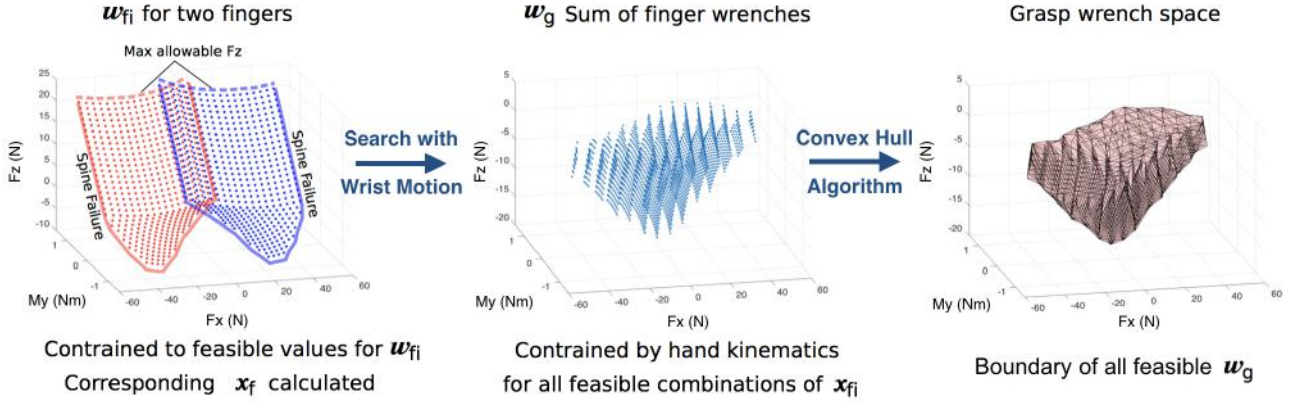
Fig. 9: Floating-wrist wrench space computation procedure. (1) Compute $(\mathcal{W}_{fi}, \mathcal{X}_{fi})$ for every finger i using the forward approach in Section 5.4. Point clouds of feasible wrenches for two opposed fingers are constrained by spine tile failure at any phalanx or excessive compressive normal force, F_z relative to the palm frame. (2) Feasible grasp wrenches are searched with incremental wrist motions, and constrained by hand kinematics. Determine the minimal size of search space for x_g by testing x_g sparsely with increasing range until the corresponding x_{fi} of each finger fully covers the solution space $\mathcal{X}_{fi}$. Search for every valid w_g, such that its corresponding $(x_{f1}, x_{f2}, \dots x_{fn})$ all stay within $(\mathcal{X}_{f1}, \mathcal{X}_{f2}, \dots \mathcal{X}_{fn})$. Sum up every $(w_{f1}, w_{f2}, \dots w_{fn})$ corresponding to the valid set of $(x_{f1}, x_{f2}, \dots x_{fn})$ to obtain the points cloud that approximates the wrench space $\mathcal{W}_g$. (3) Find the outer boundary of the point cloud using convex hull algorithm so that it can be used to solve maximum wrench limit along any given wrench direction.

space by sweeping over all possible wrench directions. For SpinyHand, new approaches are possible for the two types of grasp failure.

For applications where *fixed-wrist* behavior is desirable, the tendon force of each finger can be controlled to generate a pre-planned wrench for a given robot motion such that the pose of the fingers with respect to the palm remains fixed. The wrench space in such a scenario is defined by Eqn. 9, 10 and 14:

$$W = \{w_g | w_g = o + \sum_{i=1}^{n} f_{ti} v_i, \ 0 \le f_{ti} \le f_{ti(max)}\}$$

$$\text{where} \quad o = \sum_{i=1}^{n} W_{fi} c_{sysi}, \quad v_i = W_{fi} c_{acti} \tag{16}$$

The wrench space of an n-finger hand is a polyhedron spanned by vector v_i for each finger, with one of the vertex locations at o. For the example of a planar, opposed-finger gripper, the wrench space reduces to a parallelepiped in (F_x, F_z, M_y) of the hand. When palm contact may apply positive forces to the grasped surface along the z-axis, the wrench space becomes a volume swept from the parallelepiped to its projection on plane $z = 0$. More fingers expand the wrench space hull to have larger volume and cover more dimensions.

For robots in force-based arm control, SpinyHand can passively, robustly anchor onto surfaces with stationary finger motors. In this case, the wrench space is limited by *floating-wrist* grasp failure. It can be computed using the inverse solution of Section 5.4.2 while searching the wrench direction over a 6D unit sphere. This computationally expensive method (O^7 of the inverse solution) motivates a new method summarized in Fig. 9.

A single finger wrench space point cloud $\mathcal{W}_f$ can be computed by searching for limiting finger positions x_f corre-

sponding to limiting contact forces:

$$\mathcal{W}_f = \{w_f | w_f = W_f f_c, \ f_c \le f_s\} \tag{17}$$

The resulting f_c depends only on x_f in this approach. The search space should be large enough such that the boundaries of $\mathcal{W}_f$ are cases of $f_c = f_s$. The valid set (defined when $f_c \le f_s$) of x_f corresponding to $\mathcal{W}_f$ is denoted $\mathcal{X}_f$. For an n-finger hand, a pair of $(\mathcal{W}_{fi}, \mathcal{X}_{fi})$ can be computed for each finger individually. However, every set of $(x_{f1}, x_{f2}, \dots x_{fn})$ in $(\mathcal{X}_{f1}, \mathcal{X}_{f2}, \dots \mathcal{X}_{fn})$ must satisfy the geometry constraints of the hand, expressed in terms of the palm. The sum of $(w_{f1}, w_{f2}, \dots w_{fn})$ corresponding to each valid set forms the discretized representation of $\mathcal{W}_g$. While this new search problem requires O^{6n} computation time, it can be reduced to O^6 by transforming the search space to x_g space (because every x_{fi} is determined by x_g). Note that efficiency of the algorithm is sensitive to size and sparsity of the discretized search space. The intermediate step of finding $\mathcal{X}_f$ helps reduce the size of the search space for x_g. Populating $(\mathcal{W}_f, \mathcal{X}_f)$ with points from (w_g, x_g) describes every possible wrench on the finger bases and the palm. In summary, we compute the intersection set of the x_g, subject to kinematic constraints, that correspond to the various limiting x_f and their associated f_c, and then using the resulting volume of X_g to compute the associated W_g.

5.7 Contact Breakage

The above model assumes contacts exist on every phalanx and defines grasp failure as spine slippage at any contact. At times, higher wrench limits may be achieved if the weakest contact's loading limit is small. For example, the proximal phalanx can easily lose contact when the hand is loaded away from a large curvature surface, yet the overall grasp can still succeed. In some cases, such as the
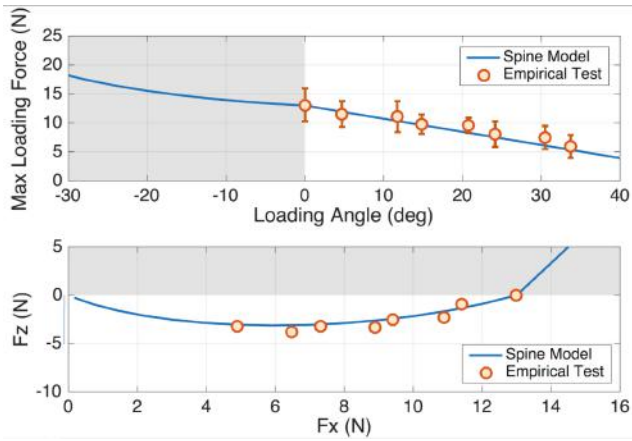
Fig. 10: Spine attachment force limit curve of a phalanx spine tile. Each point represents data of at least 5 measurements. The results are presented in polar coordinates (top) and Cartesian coordinates (bottom). Regions shaded in gray represent compressive (positive) contact forces, and are not of main interest in this study. The loading angle is defined as the angle between F_x and the loading force direction, while maximum loading force magnitude is defined as $\sqrt{F_x^2 + F_z^2}$.
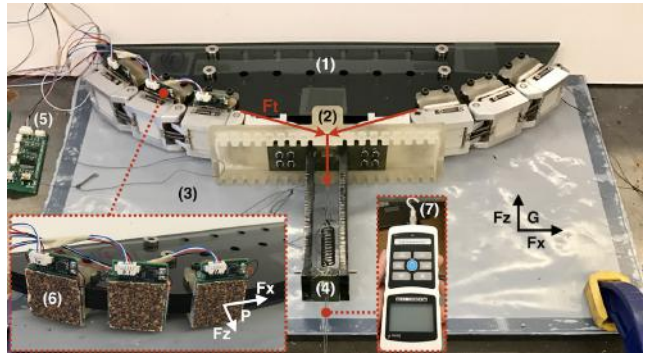

Fig. 11: Experimental setup for measuring phalanx contact forces of a gripper with SpinyHand fingers: (1) interchangeable surface with set curvature (300mm diameter in the photo); (2) mounting plate for the fingers; (3) grounded board covered in PTFE film; (4) Loading frame with slots to adjust the spring length; (5) signal processing board for the sensors; (6) interchangeable contact surface covered with tactile sensors and sand paper; (7) force gauge to measure the loading force (Mark-10, Series 4). The phalanx coordinates P and global coordinates G are shown in the figure.

crimp grasp, allowing contact breakage on proximal phalanges helps form partial closure, however a common loading direction on all fingers is then required. If any of the phalanges loses contact, the system of Eqn. 6 becomes over-determined. One of the finger joints may start to move due to this imbalance until it reaches a joint limit (Fig. 8 (b)). In this case the two adjacent phalanges can be modeled as one combined link and Eqn. 6 can be solved with a smaller square matrix A. This new reduced equation system is used to model the crimp grasp in Fig. 8(a).

6 Experiments

Three sets of experiments help to verify different levels of model predictions: spine attachment limit, phalanx contact forces, and gripper wrench space. All experiments utilize coarse 36-grit sandpaper on gripping surfaces in lieu of rock for consistency and to reduce maximum forces for ease of testing. The maximum force on rock is typically 2-5 times greater [17].

6.1 Spine Attachment Limit

The spine contact model is first verified using a single tile. The tile is placed in contact with sandpaper attached to a force and torque sensor (ATI Gamma), then contact force is measured as the tile is loaded with increasing force until it slips. As seen in Fig. 10, the empirical data gathered from 70 trials match model predictions of the force limit curve in [17]. Gray regions indicate positive normal forces, where conventional Coulomb friction applies. A comparison of the data in polar and Cartesian coordinates also suggests that it is reasonable to approximate the limit curve as a straight line in Cartesian coordinates for each phalanx, to simplify characterization and computation.

6.2 Phalanx Contact Forces

A second set of experiments measures how contact forces change on each phalanx while a hand is loaded in the floating-wrist mode. For these tests, two of the fingers are mounted in a planar frame and made to contact a curved object, as seen in Fig. 11. The frame holding the fingers slides on a low-friction PTFE film as the grasp adjusts to changes in loading. Loads are applied by pulling on a cable attached to the frame, producing forces, F_x, F_z. A spring attached to each tendon provides an approximately constant grasp force for small motions.

Taking advantage of symmetry, the grasp is instrumented by having each phalangeal tile on the left finger contact an instrumented block with a thin, capacitive force/torque sensor adapted from [39]. The sensors measure contact forces and moments at 109 Hz with an accuracy of approximately 5% for 0-25 N in F_x and 0-10 N in F_z.

The testing procedure is: (i) place the fingers around the curved object and align each tile on the corresponding contact block; (ii) preload the gripper with tendon forces of 37 N; (iii) pull on the external loading cable while measuring the force with a force gage (Mark-10, Series 4, 157 Hz) until any tile slips.

As shown in Fig. 12, shear and normal forces measured at the contacts match trends predicted by the model. As the gripper initially grasps the surface, each phalanx tile slides some distance before catching on asperities. Therefore each phalanx starts with a different shear preload. As the external loading force pulls the hand away from the surface, shear contact forces increase gradually, with some oscillation due to friction in the pulley systems, as discussed in Section 5.2. Results also show that the normal components at the proximal and distal phalanges decrease, so that these contacts are likely to exceed their force limits. The middle phalanx typically stays within safe loading conditions. The exact failure condition depends on the details of spine-asperity engagement at each tile and varies somewhat on a trial by trial basis.

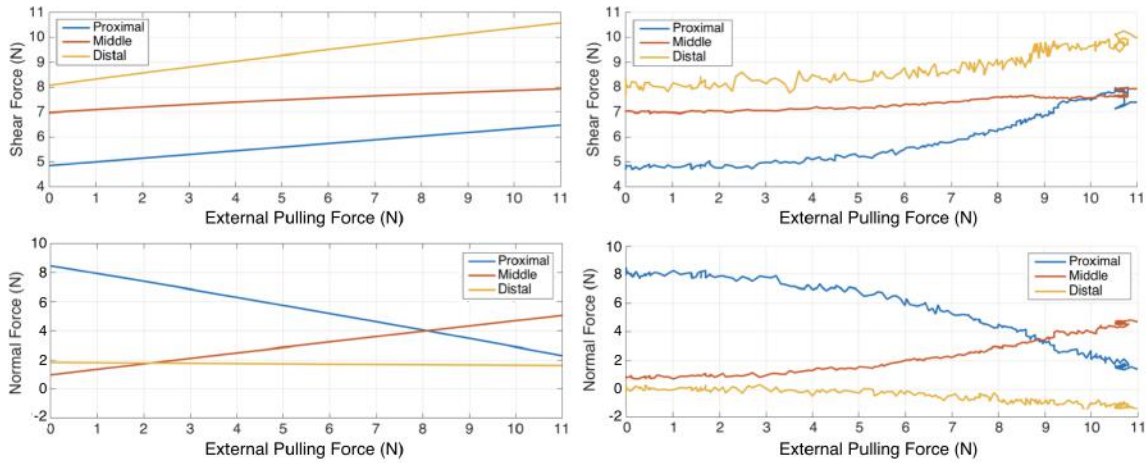The grasp model is linear and does not explain some

Fig. 12: Variation of shear (F_x) and normal (F_z) contact forces on each of the phalanges as the gripper is loaded with increasing force along the negative global F_z direction. Model predictions in the left two plots show similar trends as the actual measurements in the right two plots.
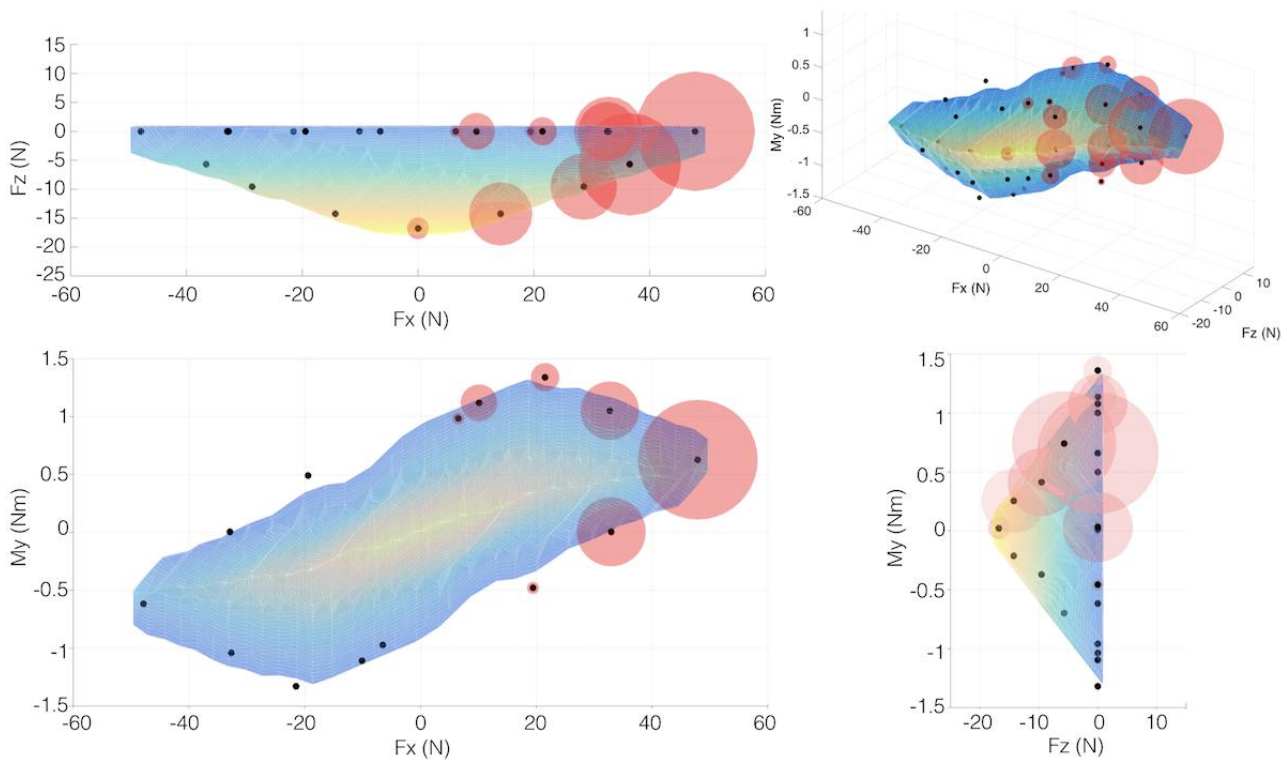

Fig. 13: Wrench space experiments and model predictions for grasping on a 300mm diameter curved surface. The wrench space hull in gradient color is numerically computed with the grasp model. The black dots are average results of 5 measurements along each wrench direction vector. The red sphere displays the standard deviation of loading force magnitude for each data point. The dots that are not covered with red spheres are mirrored data to show the complete wrench space. Prediction error on average is 10%.

observed nonlinearity in the plots, which arises from a combination of backlash and friction in the system. In addition, during these experiments, the gripper base shifts by up to 5mm, consistent with model predictions. However, in the model we assume that corresponding changes in joint angles, tendon length, and loading spring force are negligible. This is counter to the ill-conditioned property of A in Eqn. 6 (Section 5.1), which suggests that small changes in finger pose (q) can significantly alter contact forces.

6.3 Gripper Wrench Space

The experimental setup and procedure for measuring the wrench space is similar to that in Fig. 11. However, the external load cable is now attached to various points on the frame to produce a force an moment (F_x, F_z, M_y). The pulling direction is held constant as the force increases until either one of the tiles slips or the entire hand detaches. For a 300 mm diameter surface, 17 unit vector directions were selected to evenly cover the wrench space for $F_z \leq 0$ (i.e., when pulling the object away from the fingers). Five trials were repeated

for each load location. The sandpaper patches were replaced every 25 trials to reduce the effect of contact surface degradation. A lower curvature surface with a 700 mm diameter was additionally tested.

As seen in Fig. 13 for the 300 mm diameter curved surface, the negative F_z region of the wrench space has an inverted "mountain" shape. We assume symmetry in the model and reflect the empirical data points to cover the space. When one applies some positive shear force F_x, one side of the finger tiles has larger shear forces and the other side has reduced shear forces. Accordingly, the side in the $+x$ direction is closer to losing contact whereas the opposite side is not in danger of losing contact and has some margin with respect to its spine adhesion limits. Hence adding a positive moment to keep both sides firmly in contact can actually increase the overall strength of the grasp with respect to pull-out forces.

The average failure conditions match the model, albeit with variability in some cases, denoted by the radius of the red shaded region around each empirical data point. The overall deviation from the model averages 10%, and is greatest in high-wrench regions where trial-to-trial variability is highest. Grasping tests on the lower curvature surface (700 mm diameter) were conducted using two different finger tendon actuation forces, 30N and 40N; an average model error of 12% and 14% resulted respectively. In either case, the limit surfaces are smaller (it is harder to grasp a large diameter object) and the errors are somewhat larger.

7 Results

The model can predict where phalanx contact failure will likely occur first. Hence it could be useful for grasp and load planning. Figure 14 visualizes the failure modes with different color dots covering the wrench space surfaces. Grasping on more curved (smaller radius) surfaces results in a larger wrench space, and most contact failures start from the proximal phalanx. Distal phalanx failure occurs when the loading moment, M_y, is comparatively small compared with shear loading force, F_x. When grasping a large radius surface the entire wrench space is dominated by proximal phalanx failure. These results match experimental observations, and indicate that initial grasp slipping may be reduced by enhancing the proximal phalanx attachment, e.g. with a denser array of spines.

SpinyHand has a skew symmetric wrench space, for this prototype (when loaded in the plane of opposed finger actuation). One can optimize grasp attachment strength, interpreted here as either $\sqrt{F_x^2 + F_z^2}$ or M_y, by changing the applied wrench direction. Figure 14 shows that for both surface curvatures, a higher shear force to moment ratio $F_x{:}M_y$ improves point force attachment (optimal ~90:1, dashed), while a lower ratio achieves better moment resistance (optimal ~20:1, dotted). The dashed and dotted lines represent loading planes (wrench slices) that respectively correspond to the top and side views in Fig. 13. These insights can inform robot motion planning to distribute loads effectively among different end-effectors and reduce the risk of falling while climbing. In addition to active control strategies, the
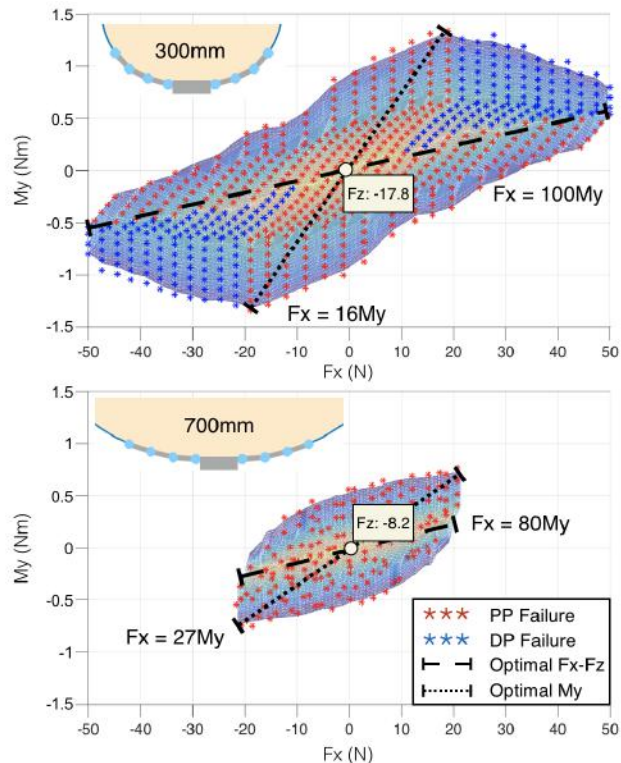

Fig. 14: Visualization of failure modes and loading configuration on two grasping conditions (300mm and 700mm diameter surfaces) that have been verified with experiments. Red and blue dots represent proximal and distal phalanx failure (PP and DP) respectively. The dash lines and dotted lines indicate optimal loading planes to achieve large resisting force and moment respectively.
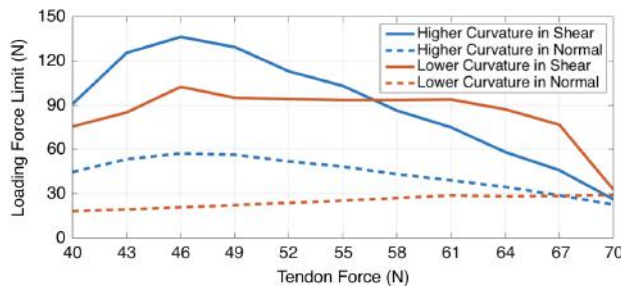

Fig. 15: Shear and normal grasp force limits for the two previously discussed surfaces with changing finger tendon forces. Blue lines: 300 diameter surface. Red lines: 700 diameter surface. The shear force is under loading configuration of $F_x = 50M_y$.

hand mechanism can be tailored to task requirements. For example, if the hand is loaded at a single point via a cable (as in these studies), the best place to anchor the loading cable for the 300 mm diameter surface is 1.1 cm away from the palm surface along the center axis of the palm (negative z direction) to produce an ideal combination of force and moment, based on the results in Fig. 14.

7.1 Parameterized Studies

Many factors influence grip strength, including surface properties, finger kinematics, and actuation control strategy. We can use the previous grasp model in simulations with var-
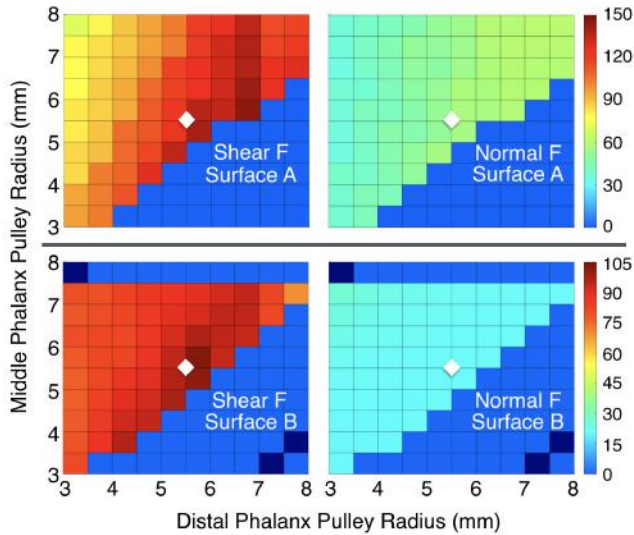
Fig. 16: Shear and normal grasp attachment force limits for the two previously discussed surfaces with changing middle and distal phalanx pulley radii and constant finger tendon force (46N). The color map shows the force magnitudes. Surface A and B are 300mm and 700mm diameter surfaces. The blue region indicates that phalanx contact failure has occurred before applying external load. The dark blue blocks are cases where the gripper ejects itself away from the surface. The white diamond is the pulley radii selections of the implemented SpinyHand.

ious hand configurations to investigate how finger actuation and transmission ratios influence grasping.

Grasp experiments maintain a constant finger tendon tension of 37 N. To investigate the effect of different tendon tensions, a batch of wrench simulations were run for the opposed two-finger gripper on the curved 300mm and 700mm diameter curvatures, now covered in fine concrete surfaces (higher spine engagement strength [17]). A range of finger tendon forces were tested under the loading configuration $F_x = 50M_y$. As shown in Fig. 15, moderate finger tendon forces help expand the wrench space. Large tendon actuation may help obtain better normal attachment on lower curvature surfaces, but gradually reduces shear loading capability. In general, the wrench space for a low curvature surface is both lower and less sensitive to tendon force variations. On more curved surfaces, the normal force component of the finger contact contributes substantially to attachment. However, it also can lead to premature failure at the distal or proximal phalange. In general, controlling the tendon force is more important for objects with higher curvature.

The SpinyHand fingers contain numerous load-sharing elements that can be adjusted, including joint stiffnesses and preloads, prismatic phalanx stiffnesses and preloads, and joint and tile pulley radii. Based on Eqn. 14, the system component c_{sys} determined by the spring elements contributes to only the initial states of the grasp. As finger tendon force increases, the actuation component c_{act} will eventually dominate the contact forces. For a given tendon tension, this c_{act} depends only on the pulley radii r of each finger joint and the tile pulley radii which determine f_p. These are arrays consisting of n scalars for an n-phalanx finger. In the finger plane, tendon force directly determines shear components of

the contact forces; the corresponding normal force components are affected by varying these design parameters. Considering the inverted matrix A, change in only one of the n degree of freedom variables r and f_p will adjust every contact force. As it is practically easier to adjust the pulley radii vector r (as compared to f_p), they are considered here as a design parameter for optimizing grasp performance. The remaining design parameters remain useful for tuning finger behaviors, such as the closing sequence.

Wrench simulations were conducted while varying middle and distal joint pulley radii. The proximal pulley radius is fixed to be 5.5 mm, as in the SpinyHand prototype. The radius of the distal joint pulley should not be larger than the middle joint pulley, as this condition could lead to fixed-wrist grasp failure due to finger actuation (dark blue regions). Lowering the tendon force may help decrease the size of the failure regions, but also reduces the attachment force limit according to Fig. 15. In order to achieve adequate performance on both the 300 mm and 700 mm surfaces, SpinyHand employs pulley radii represented by white diamonds in Fig. 16.

These results provide initial insights into how design and control can be influenced by an understanding of multifinger spine attachment for rock climbing.

8 Conclusion

This work introduces a multi-finger hand designed for human-scale robots climbing on steep, rocky terrain. Inspired by human rock climbing techniques, the hand can perform a variety of grasp types, such as sloper or pinch grasps, or cling to an edge with its fingernails. Dense arrays of spines improve contact properties at each phalange and in the palm. The tiles are connected by tendons and float on linear tracks, ensuring load-sharing along each finger. The phalange design particularly improves gripping robustness on challenging low-curvature surfaces by allowing each contact to support large shear loads. A modest amount of transmission friction can actually be helpful because it allows those tiles with the strongest and stiffest contacts to take slightly larger loads.

Contact force and wrench space grasp models are developed, taking advantage of the load-sharing among phalanges to greatly accelerate the solution. A fast wrench-space computation method is presented, searching for the space of limiting compliant motions of the wrist, subject to kinematic constraints, and then computing the corresponding forces. Although it is challenging to test the entire hand to failure due to the very high forces involved, experiments were conducted with two fingers in a symmetric planar grasp using measured applied loads and contact forces. The results match numerical predictions, with some variability due to friction, backlash and a modeling assumption that small motions do not significantly affect the kinematics of the fingers.

Simulations of the hand on small- and large-curvature objects are presented, and allow one to examine different tendon actuation strategies and the effects of varying design parameters such as pulley radii. In general, the wrench space of allowable external loads becomes smaller as surfaces be-

come increasingly flat and the sensitivity to variations in actuating tendon tension become less.

8.1 Future work

While the grasp model is generalized for 6D wrenches, experimental validation has examined only planar grasps. Future work will investigate intermediate orientations of the rotated outer fingers (instead of just 0° or 180°). As the grasp model continues to be validated in these more general grasps, it also becomes useful to incorporate the grasp model into a package such as SimGrasp [40] exploring the effects of changing phalange lengths, stiffnesses, etc.

Adjustments to the hand design could improve capability and resilience. For example, there may be phases during grasping when the spines should be retracted to induce slipping contact temporarily. Pneumatic retraction of the spines could improve conformability and spine/gripper lifetime by decreasing unnecessary spine engagement. A compact clutch or brake design could additionally reduce the number of motors and overall weight of the hand [41], while including tendon tension sensors and fingerpad tactile sensors could enable new closed-loop control strategies. These updates could enable innovative gripping techniques specific to rock climbing.

The ultimate goal is to integrate this technology with the RoboSimian quadruped, resulting in new questions regarding integration of design, control, and sensitivity.

References

[1] Asbeck, A. T., Kim, S., Cutkosky, M. R., Provancher, W. R., and Lanzetta, M., 2006. "Scaling hard vertical surfaces with compliant microspine arrays". *The International Journal of Robotics Research,* **25**(12), pp. 1165–1179.

[2] Spenko, M. J., Haynes, G. C., Saunders, J. A., Cutkosky, M. R., Rizzi, A. A., Full, R. J., and Koditschek, D. E., 2008. "Biologically inspired climbing with a hexapedal robot". *Journal of Field Robotics,* **25**, pp. 223–242.

[3] Daltorio, K. A., Wei, T. E., Horchler, A. D., Southard, L., Wile, G. D., Quinn, R. D., Gorb, S. N., and Ritzmann, R. E., 2009. "Mini-whegs tm climbs steep surfaces using insect-inspired attachment mechanisms". *The International Journal of Robotics Research,* **28**(2), pp. 285–302.

[4] Sintov, A., Avramovich, T., and Shapiro, A., 2011. "Design and motion planning of an autonomous climbing robot with claws". *Robotics and Autonomous Systems,* **59**(11), pp. 1008–1019.

[5] Lynch, G. A., Clark, J. E., Lin, P.-C., and Koditschek, D. E., 2012. "A bioinspired dynamical vertical climbing robot". *The International Journal of Robotics Research,* **31**(8), pp. 974–996.

[6] Lam, T. L., and Xu, Y., 2012. "Biologically inspired tree-climbing robot with continuum maneuvering mechanism". *Journal of Field Robotics,* **29**(6), pp. 843–860.

[7] Parness, A., Frost, M., Thatte, N., King, J. P., Witkoe, K., Nevarez, M., Garrett, M., Aghazarian, H., and Kennedy, B., 2013. "Gravity-independent rock-climbing robot and a sample acquisition tool with microspine grippers". *Journal of Field Robotics,* **30**(6), pp. 897–915.

[8] Parness, A., Carpenter, K. C., and Wiltsie, N., 2015. Terrain traversing device having a wheel with micro-hooks, Mar. 17. US Patent 8,978,807.

[9] Liu, Y., Sun, S., Wu, X., and Mei, T., 2015. "A wheeled wall-climbing robot with bio-inspired spine mechanisms". *Journal of Bionic Engineering,* **12**(1), pp. 17–28.

[10] Lee, J. S., and Fearing, R. S., 2015. "Anisotropic collapsible leg spines for increased millirobot traction". In Robotics and Automation (ICRA), 2015 IEEE International Conference on, IEEE, pp. 4547–4553.

[11] Xu, F., Wang, B., Shen, J., Hu, J., and Jiang, G., 2017. "Design and realization of the claw gripper system of a climbing robot". *Journal of Intelligent & Robotic Systems*, pp. 1–17.

[12] Parness, A., Abcouwer, N., Fuller, C., Wiltsie, N., Nash, J., and Kennedy, B., 2017. "Lemur 3: A limbed climbing robot for extreme terrain mobility in space". In 2017 IEEE International Conference on Robotics and Automation (ICRA), pp. 5467–5473.

[13] Karumanchi, S., Edelberg, K., Baldwin, I., Nash, J., Reid, J., Bergh, C., Leichty, J., Carpenter, K., Shekels, M., Gildner, M., Newill-Smith, D., Carlton, J., Koehler, J., Dobreva, T., Frost, M., Hebert, P., Borders, J., Ma, J., Douillard, B., Backes, P., Kennedy, B., Satzinger, B., Lau, C., Byl, K., Shankar, K., and Burdick, J. "Team robosimian: Semi-autonomous mobile manipulation at the 2015 darpa robotics challenge finals". *Journal of Field Robotics,* **34**(2), pp. 305–332.

[14] Dai, Z., Gorb, S. N., and Schwarz, U., 2002. "Roughness-dependent friction force of the tarsal claw system in the beetle pachnoda marginata (coleoptera, scarabaeidae)". *Journal of Experimental Biology,* **205**(16), pp. 2479–2488.

[15] Asbeck, A. T., and Cutkosky, M. R., 2012. "Designing compliant spine mechanisms for climbing". *Journal of Mechanisms and Robotics,* **4**(3), pp. 031007–031007–8.

[16] Wang, S., Jiang, H., and Cutkosky, M. R., 2017. "Design and modeling of linearly-constrained compliant spines for human-scale locomotion on rocky surfaces". *The International Journal of Robotics Research,* **36**(9),

pp. 985–999.

[17] Wang, S., Jiang, H., and Cutkosky, M. R., 2016. "A palm for a rock climbing robot based on dense arrays of micro-spines". In 2016 IEEE/RSJ International Conference on Intelligent Robots and Systems (IROS), pp. 52–59.

[18] Prattichizzo, D., and Trinkle, J. C., 2016. "Grasping". In *Springer Handbook of Robotics*. Springer, pp. 955–988.

[19] Melchiorri, C., and Kaneko, M., 2016. "Robot hands". In Springer Handbook of Robotics, B. Siciliano and O. Khatib, eds., Springer International Publishing, pp. 463–480.

[20] Bicchi, A., and Kumar, V., 2000. "Robotic grasping and contact: a review". In IEEE Int. Conf. Robotics and Automation, Vol. 1, pp. 348–353.

[21] Boyd, S. P., and Wegbreit, B., 2007. "Fast computation of optimal contact forces". *IEEE Trans. Robotics,* **23**(6), Dec, pp. 1117–1132.

[22] León, B., Morales, A., and Sancho-Bru, J., 2014. *Robot Grasping Foundations*. Springer International Publishing, Cham, pp. 15–31.

[23] Jiang, H., Wang, S., and Cutkosky, M. R., 2018. "Stochastic models of compliant spine arrays for rough surface grasping". *The International Journal of Robotics Research,* **37**(7), pp. 669–687.

[24] Baril, M., Laliberté, T., Guay, F., and Gosselin, C., 2010. "Static analysis of single-input/multiple-output tendon-driven underactuated mechanisms for robotic hands". In ASME 2010 International Design Engineering Technical Conferences and Computers and Information in Engineering Conference, American Society of Mechanical Engineers, pp. 155–164.

[25] Catalano, M., Grioli, G., Farnioli, E., Serio, A., Piazza, C., and Bicchi, A., 2014. "Adaptive synergies for the design and control of the pisa/iit softhand". *The International Journal of Robotics Research,* **33**(5), pp. 768–782.

[26] Hauser, K., Wang, S., and Cutkosky, M. R., 2018. "Efficient equilibrium testing under adhesion and anisotropy using empirical contact force models". *IEEE Transactions on Robotics,* **34**(5), Oct, pp. 1157–1169.

[27] Martín, J. M., Campo, V. L. D., Román, M. L., Horrillo, J. M. G.-V., and Navarrete, J. S. G., 2013. "Description of the finger mechanical load of climbers of different levels during different hand grips in sport climbing". *Journal of Sports Sciences,* **31**(15), pp. 1713–1721.

[28] Fuss, F. K., and Niegl, G., 2008. "Instrumented climbing holds and performance analysis in sport climbing". *Sports Technology,* **1**(6), pp. 301–313.

[29] Amca, A. M., Vigouroux, L., Aritan, S., and Berton, E., 2012. "Effect of hold depth and grip technique on maximal finger forces in rock climbing". *Journal of Sports Sciences,* **30**(7), pp. 669–677.

[30] Quaine, F., Vigouroux, L., and Martin, L., 2003. "Effect of simulated rock climbing finger postures on force sharing among the fingers". *Clinical Biomechanics,* **18**(5), pp. 385 – 388.

[31] Hawkes, E. W., Jiang, H., Christensen, D. L., Han, A. K., and Cutkosky, M. R., 2017. "Grasping without squeezing: Design and modeling of shear-activated grippers". *IEEE Transactions on Robotics*.

[32] Glick, P., Suresh, S., Ruffatto III, D., Cutkosky, M., Tolley, M. T., and Parness, A., 2018. "A soft robotic gripper with gecko-inspired adhesive". *IEEE Robotics and Automation Letters*.

[33] Birglen, L., Laliberté, T., and Gosselin, C., 2008. *Underactuated Robotic Hands*, Vol. 40 of *Springer Tracts in Advanced Robotics*. Springer Berlin Heidelberg, Berlin, Heidelberg.

[34] Demers, L. A. A., and Gosselin, C., 2009. "Kinematic design of an ejection-free underactuated anthropomorphic finger". In 2009 IEEE International Conference on Robotics and Automation, pp. 2086–2091.

[35] Stuart, H., Wang, S., Khatib, O., and Cutkosky, M. R., 2017. "The Ocean One hands: An adaptive design for robust marine manipulation". *The International Journal of Robotics Research,* **36**(2), pp. 150–166.

[36] Hauser, K., Wang, S., and Cutkosky, M., 2017. "Efficient equilibrium testing under adhesion and anisotropy using empirical contact force models". In Proceedings of Robotics: Science and Systems (RSS).

[37] Cutkosky, M. R., and Kao, I., 1989. "Computing and controlling compliance of a robotic hand". *IEEE Transactions on Robotics and Automation,* **5**(2), pp. 151–165.

[38] Baraff, D., 1994. "Fast contact force computation for nonpenetrating rigid bodies". In Proc. 21st Annual Conf. Computer Graphics and Interactive Techniques, SIGGRAPH '94, ACM, pp. 23–34.

[39] Wu, X. A., Suresh, S. A., Jiang, H., Ulmen, J. V., Hawkes, E. W., Christensen, D. L., and Cutkosky, M. R., 2015. "Tactile sensing for gecko-inspired adhesion". In 2015 IEEE/RSJ International Conference on Intelligent Robots and Systems (IROS), pp. 1501–1507.

[40] Wang, S., 2016. Simgrasp: Grasp simulation package. https://bitbucket.org/shiquan/sim-grasp.

[41] Aukes, D. M., Heyneman, B., Ulmen, J., Stuart, H., Cutkosky, M. R., Kim, S., Garcia, P., and Edsinger, A., 2014. "Design and testing of a selectively compliant underactuated hand". *The International Journal of Robotics Research,* **33**(5), pp. 721–735.

9 Appendices

9.1 Design Details

As shown in Fig. 17, four brushed motors (Maxon RE25 12V) are housed inside the two halves of the palm chamber. Double bronze bushings support each motor shaft that winches a tendon to actuate each finger. Two small, brushed motors (Pololu, 0.22Nm, 320RPM, 12V) with worm drives (1:48) alter the alignment of the two outer fingers. The rotary finger base assembly (Fig. 18) also includes an angular contact bearing to resist finger moments and a thrust bearing to reduce friction caused by axial mounting force. A channel through the assembly is left for the finger tendon to come out of palm chamber. This through hole is concentric with the rotary motion axis to prevent tendon tangling.

The hand is equipped with eight analog sensors to monitor the four tendon pulley positions as well as positions and moments on the two rotary finger bases. Tendon pulley positions are tracked with four magnetic rotary encoders (RLS RMB20) installed on the back shaft of the big motors. Two pairs of magnets (hollow cylindrical for tendon to go through) and hall effect transducers are directly mounted on the worm gear to track absolute position of the rotary finger base. To prevent large impacts and torques transmitted from the finger from damaging the worm gear, a cubic magnet is installed on each of the small motor mounting plates (Fig. 17(g)) to sense the plate deflection, and thus measure the axial force created by the worm gear transmission. The motor will backdrive when torque is above certain threshold to prevent damage. The sensors are signal-conditioned by a customized four-layer PCB board (Fig. 17(c)) and read by a micro-controller (Teensy3.2) stacked on the board.

Besides sensor signal processing, the PCB board interfaces with four external motor drivers (15A nominal, for each big motor) and a dual channel motor driver (0.7A nominal, for each small motor). Power for logic and motors is regulated and transmitted through a separated region on the middle layers of the board. The compact electronics package fits inside the bottom palm chamber.

9.2 Palm Model Derivations

Force balancing equations on the tiles (Fig. 5) indicate tendon travel tendency, thus friction direction, is unknown:

$$\begin{cases} F_{t0} + F_{t1} + k_p(x - x_1) = k_1 x_1 \\ F_{t1} + F_{t2} + k_p(x - x_2) = k_2 x_2 \end{cases} \quad (18)$$

If the tendon is static and we assume contact stiffness $k_1 > k_2$, x_2 will be larger than x_1 and the tendon has the tendency to travel to the left. The force balancing equations on the
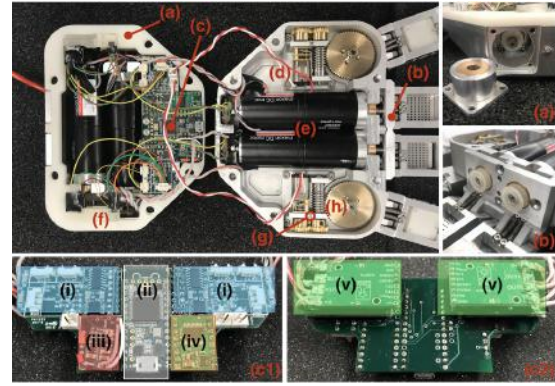

Fig. 17: Actuation and electronics design in the palm chamber: (a) double bushings shaft support for bottom chamber motors; (b) double bushing shaft support for top chamber motors; (c) 4-layer PCB board; (d) small motor and worm drive assembly; (e) big motors; (f) mounting plates for hall effect transducers to measure rotary finger position and torque; (g) cubic magnet for torque sensing and (h) worm gear mounted to the finger base and magnet for its position sensing. More details about the 4-layer PCB board are in front view (c1): (i) sensor signal conditioning circuits; (ii) Teensy 3.2 micro-controller; (iii) power regulator, (iV) dual channel small motor driver and in rear view (c2) where (v) are four stacked big motor drivers.
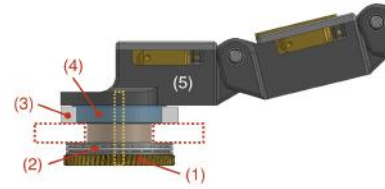

Fig. 18: Rotary finger base design: (1) worm gear; (2) thrust bearing; (3) compact cross-roller bearing (transparent mode); (4) finger base adapting plate; (5) finger base phalanx. The rectangular areas with dotted line show the solid part of the palm wall pinched by the finger base assembly.

pulleys becomes:

$$\begin{cases} (1 + \mu/2)F_{t1} = (1 - \mu/2)F_{t0} \\ (1 + \mu/2)F_{t2} = (1 - \mu/2)F_{t1} \end{cases} \quad (19)$$

Both ends of the tendon are fixed to the palm, and displacements of the palm and two tiles should satisfy: $x_1 + x_2 = 2x$. Total force on the palm is the sum of contact forces on each tile $F_1 = k_1 x_1$ and $F_2 = k_2 x_2$, and can be solved using the above equations.

9.3 Tendon Friction

When the hand is settled statically on a surface, the tendon cannot freely slide around the joint pulleys due to friction; the local tension varies along the finger tendon until force exceeds static friction. We assume the tendon tension is constant along the portion of tendon within the same phalanx. As a loading force on the wrist is applied, the hand

configuration x_g and finger joint positions q will change. If the spine tile remains stationary with respect to the phalanx, it has to travel with respect to the surface. The displacement of tile tangential to the surface on phalanx i is denoted by δx_{ci}. However, as finger joints rotate slightly, the joint pulleys either wind or unwind the finger tendon. The resulted variation on local tendon length also changes the spine tile position with respect to the phalanx by δl_{ci}. The actual tile displacement with respect to the contact surface becomes $(\delta x_{ci} + \delta l_{ci})$. Tile displacement deforms the spines and surface in shear, inducing an additional change in tangential contact forces on phalanx i:

$$\delta f_{ci} = (\delta x_{ci} + \delta l_{ci})k_{ci} \tag{20}$$

where k_{ci} is the contact stiffness between the phalanx frame. Surface compliance is empirically characterized.

9.4 Simplified Spine Model

3D spine tile attachment force limits are captured with probability-based model [16] solved with the Monte Carlo Method. For better efficiency, we simplify the contact model before integrating it to the grasp model. As empirically found in [16,17], attachment is approximately linear with the loading angle. This property allows the limit curve on the same loading plane to be linear fitted:

$$\begin{cases} f_s = f_{smax} - k_{slp}\phi; \\ k_{slp} = (f_{smax} - f_{smin})/\phi_{max}; \end{cases} \tag{21}$$

where f_{smax} and f_{smin} are the maximum and minimum empirical tile attachment, ϕ is the force loading angle on the spine tile and ϕ_{max} is the loading angle corresponding to f_{smin}.

10 Listing of figure captions

Figure 1 on page 2: SpinyHand grasping a pumice rock. The contact areas are covered in microspines to support large tangential forces.

Figure 2 on page 3: (left) SpinyHand CAD rendering shows 22 spine-laden tiles in yellow distributed among 4 independent fingers and a palm. (right) Rock climbing techniques (a-d): (a) sloper grasp on a gently curved surface; (b) open hand/half crimp grasp on an edge; (c) pinch grasp on a narrow feature; (d) pose between a sloper grasp and pinch. (d) is not commonly used by human rock climber but can be helpful for SpinyHand to envelop large-curvatures.

Figure 3 on page 3: Spine tile design: (1) sliding block for prismatic motion of the finger spine tile along x axis; (2) fixed pulley (horizontal metal rod); (3) groove for tendon routing; (4) sliding channel for palm tile; (5) fixed pulley (vertical metal rod). The red arrow indicates the sliding and loading direction. The tile coordinates are consistent with the finger phalanx coordinates P.

Figure 4 on page 4: Diagram and pictures of the finger: (1) fingernail; (2) spine tile; (3) joint pulley; (4) phalanx extension spring; (5) phalanx frame; (6) phalanx pulley; (7) joint extension spring. F_t is the tendon force. The tendon (red) routes around each joint pulley and phalanx pulley, so that F_t simultaneously curls the finger and slides the spine tile along the phalanx.

Figure 5 on page 4: Left: Palm experiment setup. Right: diagram of a 2-tile system. Parts with boundaries or shades in the same color are mounted together as single moving parts. Two tiles in gray are preloaded by springs (stiffness k_p) mounted to a moving palm frame in red. The tiles have contact stiffness k_1 and k_2 with respect to the ground in blue. A tendon routes over pulleys on the tile (gray) and palm frame (red). Local tendon tensions F_{t1} and F_{t2} may be different due to friction on pulleys between adjacent tiles. x_1, x_2 and x are global displacements of the tiles and palm frame respectively.

Figure 6 on page 5: Predicted and experimental maximum load of a two-tile system. Horizontal axis shows the contact spring configurations (springs 1, 2 and 3 have stiffness of 1.4, 2.2 and 4.9N/mm respectively). Five measurements are conducted for each spring configuration. The percentage in red shows how much friction can improve the loading capacity.

Figure 7 on page 5: Empirical maximum load of a four-tile system with and without friction. Horizontal axis shows the contact stiffness spring configurations, with the spring type sequence starting from the left.

Figure 8 on page 5: Three coordinates are used in the hand model: 1) palm (global) coordinates G; 2) finger coordinates F; 3) phalanx coordinates P. Blue dots indicates the contact locations. c_i and q_i are contact forces and joint angles. A third finger is behind the grasping surface and therefore displayed with dotted lines. The top diagrams show: (a) crimp grasp with only distal phalanx contact; (b) pinch/sloper grasp with proximal contacts broken.

Figure 9 on page 8: Floating-wrist wrench space computation procedure. (1) Compute $(\mathcal{W}_{fi}, \mathcal{X}_{fi})$ for every finger i using the forward approach in Section 5.4. Point clouds of feasible wrenches for two opposed fingers are constrained by spine tile failure at any phalanx or excessive compressive normal force, F_z relative to the palm frame. (2) Feasible grasp wrenches are searched with incremental wrist motions, and constrained by hand kinematics. Determine the minimal size of search space for x_g by testing x_g sparsely with increasing range until the corresponding x_{fi} of each finger fully covers the solution space $\mathcal{X}_{fi}$. Search for every valid w_g, such that its corresponding $(x_{f1}, x_{f2}, \ldots x_{fn})$ all stay within $(\mathcal{X}_{f1}, \mathcal{X}_{f2}, \ldots \mathcal{X}_{fn})$. Sum up every $(w_{f1}, w_{f2}, \ldots w_{fn})$ corre-

sponding to the valid set of $(x_{f1}, x_{f2}, \ldots x_{fn})$ to obtain the points cloud that approximates the wrench space $\mathcal{W}_g$. (3) Find the outer boundary of the point cloud using convex hull algorithm so that it can be used to solve maximum wrench limit along any given wrench direction.

Figure 10 on page 9: Spine attachment force limit curve of a phalanx spine tile. Each point represents data of at least 5 measurements. The results are presented in polar coordinates (top) and Cartesian coordinates (bottom). Regions shaded in gray represent compressive (positive) contact forces, and are not of main interest in this study. The loading angle is defined as the angle between F_x and the loading force direction, while maximum loading force magnitude is defined as $\sqrt{F_x^2 + F_z^2}$.

Figure 11 on page 9: Experimental setup for measuring phalanx contact forces of a gripper with SpinyHand fingers: (1) interchangeable surface with set curvature (300mm diameter in the photo); (2) mounting plate for the fingers; (3) grounded board covered in PTFE film; (4) Loading frame with slots to adjust the spring length; (5) signal processing board for the sensors; (6) interchangeable contact surface covered with tactile sensors and sand paper; (7) force gauge to measure the loading force (Mark-10, Series 4). The phalanx coordinates P and global coordinates G are shown in the figure.

Figure 12 on page 10: Variation of shear (F_x) and normal (F_z) contact forces on each of the phalanges as the gripper is loaded with increasing force along the negative global F_z direction. Model predictions in the left two plots show similar trends as the actual measurements in the right two plots.

Figure 13 on page 10: Wrench space experiments and model predictions for grasping on a 300mm diameter curved surface. The wrench space hull in gradient color is numerically computed with the grasp model. The black dots are average results of 5 measurements along each wrench direction vector. The red sphere displays the standard deviation of loading force magnitude for each data point. The dots that are not covered with red spheres are mirrored data to show the complete wrench space. Prediction error on average is 10%.

Figure 14 on page 11: Visualization of failure modes and loading configuration on two grasping conditions (300mm and 700mm diameter surfaces) that have been verified with experiments. Red and blue dots represent proximal and distal

phalanx failure (PP and DP) respectively. The dash lines and dotted lines indicate optimal loading planes to achieve large resisting force and moment respectively.

Figure 15 on page 11: Shear and normal grasp force limits for the two previously discussed surfaces with changing finger tendon forces. Blue lines: 300 diameter surface. Red lines: 700 diameter surface. The shear force is under loading configuration of $F_x = 50 M_y$.

Figure 16 on page 12: Shear and normal grasp attachment force limits for the two previously discussed surfaces with changing middle and distal phalanx pulley radii and constant finger tendon force (46N). The color map shows the force magnitudes. Surface A and B are 300mm and 700mm diameter surfaces. The blue region indicates that phalanx contact failure has occurred before applying external load. The dark blue blocks are cases where the gripper ejects itself away from the surface. The white diamond is the pulley radii selections of the implemented SpinyHand.

Figure 17 on page 15: Actuation and electronics design in the palm chamber: (a) double bushings shaft support for bottom chamber motors; (b) double bushing shaft support for top chamber motors; (c) 4-layer PCB board; (d) small motor and worm drive assembly; (e) big motors; (f) mounting plates for hall effect transducers to measure rotary finger position and torque; (g) cubic magnet for torque sensing and (h) worm gear mounted to the finger base and magnet for its position sensing. More details about the 4-layer PCB board are in front view (c1): (i) sensor signal conditioning circuits, (ii) Teensy 3.2 micro-controller, (iii) power regulator, (iV) dual channel small motor driver and in rear view (c2) where (v) are four stacked big motor drivers.

Figure 18 on page 15: Rotary finger base design: (1) worm gear; (2) thrust bearing; (3) compact cross-roller bearing (transparent mode); (4) finger base adapting plate; (5) finger base phalanx. The rectangular areas with dotted line show the solid part of the palm wall pinched by the finger base assembly.

11 Listing of table captions

No tables are included in this paper.